Conference on Modelling Fluid Flow (CMFF'22)
The 18th International Conference on Fluid Flow Technologies
Budapest, Hungary, August 30-September 2, 2022

Resolving sub-kolmogorov bubble dynamics in turbulent flows: Formulation of a multiscale numerical framework

Niklas HIDMAN[1], Henrik STRÖM[2], Srdjan SASIC[3], Gaetano SARDINA[4]

[1] Corresponding Author. Chalmers University of Technology, Department of Mechanics and Maritime Sciences-Division of Fluid Dynamics, Gothenburg, Sweden. E-mail: niklas.hidman@chalmers.se
[2] Chalmers University of Technology, Department of Mechanics and Maritime Sciences-Division of Fluid Dynamics, Gothenburg, Sweden. E-mail: henrik.strom@chalmers.se
[3] Chalmers University of Technology, Department of Mechanics and Maritime Sciences-Division of Fluid Dynamics, Gothenburg, Sweden. E-mail: srdjan@chalmers.se
[4] Chalmers University of Technology, Department of Mechanics and Maritime Sciences-Division of Fluid Dynamics, Gothenburg, Sweden. E-mail: sardina@chalmers.se

ABSTRACT

Bubbly flows are important in a range of industrial and natural processes. Still, accurately predicting the flow dynamics at industrial scales is an immense challenge, mainly because of the multiscale nature of processes occurring at bubble (micro/millimetre) scales interacting with processes at industrial scales (meters). In this work, a multiscale numerical framework is formulated that couples a macro- and a microscale fluid dynamics solver to study such interactions. The former solver predicts the turbulent liquid phase, and the latter captures the bubble dynamics in response to the turbulent fluctuations. The framework handles arbitrary gas/liquid density ratios and uses a Moving Reference Frame method that follows fast-rising bubbles due to high-density ratios and gravitational forces. The framework predicts realistic bubble dynamics, considering the turbulent liquid fluctuations that modify the bubble shapes and alter their motion. Several simulation cases are performed with different surface tensions and show bubble dynamic processes that are even faster than the Kolmogorov times. The numerical framework can be used with any general DNS technique that handles two-phase flows to treat droplets, bubbles or particles in laminar and turbulent flows.

Keywords: Bubbles, DNS, Moving reference frame, Multiphase flows, Multiscale method, Turbulence

NOMENCLATURE

C_D	$[-]$	drag force coefficient
D	$[m]$	bubble diameter
Eo	$[-]$	Eötvös number
Ga	$[-]$	Galilei number
K_P	$[s^{-2}]$	proportional coefficient
Re	$[-]$	Reynolds number
S	$[s^{-1}]$	strain rate tensor
T_D	$[s]$	derivative coefficient
T_I	$[s]$	integral coefficient
U	$[m/s]$	linearised velocity field
v	$[m/s]$	bubble velocity
a	$[m/s^2]$	acceleration
c	$[-]$	volume fraction field
e	$[m]$	error value
f	$[m/s^2]$	random forcing
g	$[m/s^2]$	gravitational acceleration
p	$[Pa]$	pressure field
t	$[s]$	time
u	$[m/s]$	velocity field
x	$[m]$	spatial coordinate
$\hat{n}$	$[-]$	interface normal
β	$[-]$	density ratio
χ	$[-]$	bubble aspect ratio
δ	$[-]$	Kronecker delta
ϵ	$[-]$	Levi-Civita symbol
η	$[m]$	Kolmogorov length scale
κ	$[m^{-1}]$	curvature
λ	$[m]$	Taylor length scale
μ	$[Pa\ s]$	dynamic viscosity
ν	$[m^2/s]$	kinematic viscosity
ω	$[s^{-1}]$	vorticity
ϕ	$[^\circ]$	bubble orientation angle
ρ	$[kg/m^3]$	density
σ	$[N/m]$	surface tension
τ	$[s]$	time scale
ε	$[m^2/s^3]$	dissipation rate

Subscripts and Superscripts

b	bubble
e	external flow
g	gas
l	liquid

mrf	moving reference frame
r	ratio
i, j, k	spatial indices
(1)	linear field
$*$	non-dimensional
0	initial value
$\wedge$	relative to the MRF

1. INTRODUCTION

Bubbly flows are important in various industrial and natural processes such as chemical reactors, nuclear reactors, heat exchangers and atmosphere-ocean exchanges. This type of multiphase flow is characterised by good heat and mass transfer properties without the need for mechanical mixing and therefore require lower operating and maintenance costs [1]. To understand and design such systems, it is crucial to predict the dynamics of bubbles and how the bubbles affect the liquid phase. However, those dynamics are not yet fully understood, and reliable models for the dynamics are still needed [2].

The main challenges of modelling multiphase flows are their multiscale nature, where phenomena occurring at the smallest scales of the order of a bubble diameter (micro-/millimetres) affect the macroscales of the order of the entire system (meters) and vice versa [3]. Because of this large range of interacting scales, even the most advanced experimental or numerical methods cannot capture all relevant dynamics in industrial systems.

Currently, standard modelling methods for multiphase flows are based on a bottom-up hierarchical strategy [4]. This strategy aims to parameterise the relevant physical phenomena starting from the small to the large scales of the system using different techniques.

At the smallest scales, the dynamics and deformation of every single bubble can be resolved on an Eulerian grid (bubble-resolved DNS) [5, 6, 7]. However, this microscopic approach requires a grid size much smaller than the bubble diameter and involves a high computational cost. Furthermore, it is only feasible to simulate computational domains of the order of several bubble diameters because of the high cost. Nevertheless, using the microscopic approach, makes it possible to formulate models for small-scale bubble phenomena such as interfacial force coefficients, breakup and coalescence criteria, bubble shape and deformation characteristics. In the bottom-up modelling strategy, these models are then used in larger-scale (macroscopic) simulation methods such as the Eulerian–Lagrangian (EL) or Eulerian–Eulerian (EE) frameworks that consequently do not resolve the smallest scales.

Although the bottom-up hierarchical modelling strategy accounts for the effects of small-scale phenomena on the larger scales, it does not consider the multiscale coupling present in multiphase flows. For example, small-scale dynamics such as the bubble deformation and motion are, in reality, influenced by, and interact with, unsteady intermittent turbulent fluctuations in the liquid phase that originate at larger scales.

To understand and model the influence of the large-scale turbulent fluctuations on the small scale bubble dynamics, there is still a need to develop numerical frameworks where the bubbles are exposed to realistic turbulent fluctuations. At the same time, the framework must still be able to fully resolve the bubble dynamics occurring at scales smaller than their diameter.

In this paper, a multiscale numerical framework is formulated that captures the small-scale bubble dynamics in response to an external turbulent flow. Specifically, the multiscale framework predicts the large-scale characteristics of turbulence and impose a more realistic flow around a bubble whose size is comparable to or smaller than the Kolmogorov length scale $\eta = (\nu^3/\varepsilon)^{1/4}$, where ν is the liquid kinematic viscosity, and ε is the turbulent kinetic energy dissipation rate. The microscale bubble dynamics is resolved using a Volume of Fluid (VOF) solver with an unsteady external flow field sampled from a Lagrangian bubble trajectory. The Lagrangian bubble is tracked in a macroscopic pseudospectral solver that simulates homogeneous isotropic turbulence. This framework is an extension of the multiscale approach by [8] to bubbles with arbitrary density ratios between the phases and where the turbulent signal from the macroscale simulation is sampled following a Lagrangian bubble rather than a passive tracer. Additionally, the computational speed of the methodology is increased by at least two orders of magnitude by using additional body forces proportional to the rate of change of the turbulent external flow field. Therefore, the approach in this work does not require any computationally expensive sub-iterations between time steps.

To account for the relative velocity between the phases, induced by the density difference and the gravitational force, the reference frame is changed in the microscopic solver to one moving with the bubble. The moving reference frame (MRF) is non-inertial and consequently introduces an additional term in the Navier–Stokes equations proportional to the bubble acceleration [9]. To follow the motion of the bubble, the MRF acceleration is determined using a Proportional Integral Derivative (PID)-controller based on the bubble displacement from its initial MRF position (P and I parts) and the bubble velocity relative to the MRF (D part).

The PID-controlled MRF approach is a combination of the MRF methods used by [10, 11] that updated the velocity of the MRF using the particle volume-averaged velocity, [12] that updated the velocity of the MRF based on the bubble displacement from its initial position and the approach used by [13] that kept the bubble in its initial position by applying a PID-controlled artificial body force. By determining the MRF acceleration using a PID-controller, the

MRF accelerates smoothly and potential numerical drifts of the bubble are minimised while still allowing the bubble to move freely.

The paper starts with an outline of the numerical framework and then provides a few simulation results of a rising bubble in homogeneous isotropic turbulence to show the capabilities of the framework.

2. NUMERICAL METHODOLOGY

The multiscale framework consists of two coupled fluid dynamics solvers. A macroscopic Eulerian-Lagrangian solver generates a homogeneous isotropic turbulent flow and samples the undisturbed liquid velocity and gradients along a Lagrangian rising bubble trajectory. The sampled turbulent signals are used to impose a fluctuating velocity field in the microscopic framework. This approach makes it possible to study the microscopic bubble dynamics in response to the macroscopic turbulent fluctuations. A detailed description and validation of the multiscale framework can be found in [3].

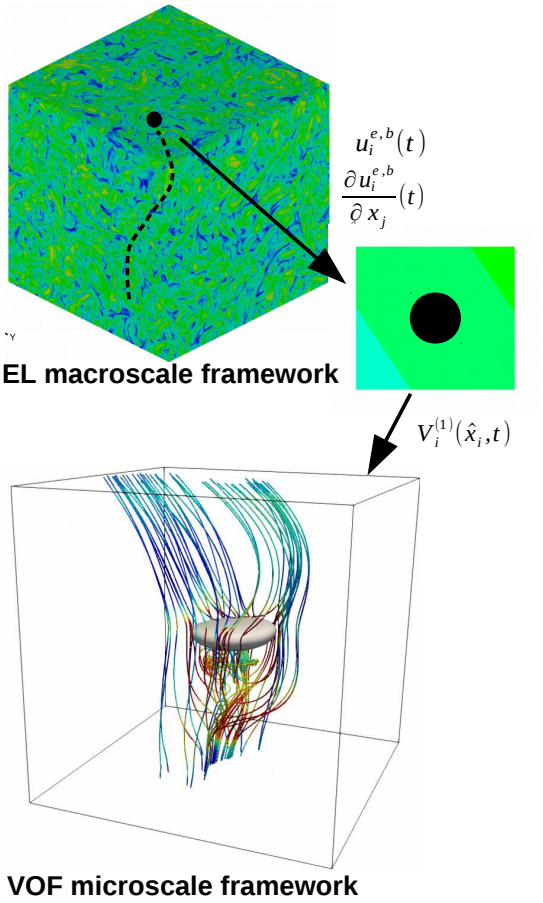

Figure 1. Illustration of the multiscale framework. Turbulent liquid fluctuations are sampled following a spherical Lagrangian bubble in the macroscale simulation. Based on these signals, a linearised unsteady flow field is imposed on the microscale simulation. The contour levels represents the liquid vorticity magnitude.

2.1. Macroscale Eulerian-Lagrangian (EL) solver

A pseudo-spectral solver is used to simulate the external homogeneous isotropic turbulent liquid flow. At low bubble volume fractions, the flow satisfies the incompressible Navier-Stokes equations according to

$$\frac{\partial u_i^{\mathrm{e}}}{\partial x_i^{\mathrm{e}}} = 0\,, \tag{1}$$

$$\frac{Du_i^{\mathrm{e}}}{Dt} = \frac{\partial u_i^{\mathrm{e}}}{\partial t} + u_j^{\mathrm{e}}\frac{\partial u_i^{\mathrm{e}}}{\partial x_j^{\mathrm{e}}} = -\frac{1}{\rho_{\mathrm{l}}}\frac{\partial p^{\mathrm{e}}}{\partial x_i^{\mathrm{e}}} + \nu\frac{\partial^2 u_i^{\mathrm{e}}}{\partial x_j^{\mathrm{e}}\partial x_j^{\mathrm{e}}} + f_i \tag{2}$$

where t and x_i^{e} are the time and space coordinates, u_i^{e} and p^{e} are the liquid velocity and pressure, ρ_{l} is the liquid density, and f_i is a random forcing that maintains the turbulent velocity at a statistically steady state. The Eqs. (1)-(2) are solved in the Fourier space using a fast Fourier transform.

The bubble evolution is tracked in a Lagrangian reference frame with the following forces included: drag, buoyancy, gravity, added mass, pressure gradient and lift. The bubble motion is computed by

$$\frac{dx_i^{\mathrm{b}}}{dt} = v_i^{\mathrm{b}}, \tag{3}$$

$$\frac{dv_i^{\mathrm{b}}}{dt} = \beta\frac{Du_i^{\mathrm{e}}}{Dt} + \frac{u_i^{\mathrm{e}} - v_i^{\mathrm{b}}}{\tau_{\mathrm{b}}}f(Re_{\mathrm{b}}) + (1-\beta)g\delta_{i3} + \\ - \epsilon_{ijk}(v_j^{\mathrm{b}} - u_j^{\mathrm{e}})\omega_k, \tag{4}$$

where x_i^{b} is the position of the bubble, v_i^{b} is the bubble velocity, $\beta = 3\rho_{\mathrm{l}}/(\rho_{\mathrm{l}} + 2\rho_{\mathrm{g}})$ is the density ratio and ρ_{g} is the bubble density, $\tau_{\mathrm{b}} = D^2/8\nu\beta$ is the bubble relaxation time and D is the diameter of the bubble, g is the gravitational acceleration, δ is the Kronecker delta and ϵ is the Levi-Civita symbol, ω is the liquid vorticity at the position of the bubble. $f(Re_{\mathrm{b}})$ is the nonlinear correction for the drag depending on the bubble Reynolds number $Re_{\mathrm{b}} = |u_i - v_i^{\mathrm{b}}|D/\nu$ according to [14, 15]

$$f(Re_{\mathrm{b}}) = 1 + \frac{Re_{\mathrm{b}}}{8 + \frac{1}{2}\left(Re_{\mathrm{b}} + 3.315\sqrt{Re_{\mathrm{b}}}\right)}. \tag{5}$$

The added mass and the lift coefficients is assumed equal to 0.5. More numerical details regarding the macroscale EL solver can be found in [16, 17].

2.2. Microscale Volume of Fluid (VOF) solver

Here, a brief outline of the microscale numerical framework is given. For more details and validation please refer to [3].

The problem of a single bubble rising due to buoyancy in a liquid is entirely defined by four dimensionless parameters [6]: the Galilei number $Ga = \rho_{\mathrm{l}}\sqrt{gD}D/\mu_{\mathrm{l}}$ that is the ratios of buoyancy to viscous forces, the Eötvös number $Eo = \rho_{\mathrm{l}}gD^2/\sigma$ that is the ratios of buoyancy to surface tension

forces, the density ratio $\rho_r = \rho_l/\rho_g$ and the dynamic viscosity ratio $\mu_r = \mu_l/\mu_g$. The symbols l and g denote the liquid and the gas phases, D is the spherical equivalent bubble diameter, σ is the surface tension, and $\rho_r = 1000$ and $\mu_r = 100$ are used that approximately represents a water-air system. All variables in the microscopic solver are made non-dimensional using D, g, ρ_l and μ_l: $x_i^* = x_i/D$, $u_i^* = u_i/\sqrt{gD}$, $t^* = t/\sqrt{D/g}$, $\rho^* = \rho/\rho_l$, $\mu^* = \mu/\mu_l$, $p^* = p/(\rho_l g D)$, $g_i^* = g_i/g$ and $\kappa^* = \kappa D$.

To keep the bubble position fixed in the computational domain, a change of reference frame is made:

$$\hat{x}_i^* = x_i^* - x_{\mathrm{mrf},i}^* \,, \tag{6}$$

$$\hat{u}_i^* = u_i^* - u_{\mathrm{mrf},i}^* \,, \tag{7}$$

$$\hat{t}^* = t^* \tag{8}$$

where $\hat{x}_i^*$ is the non-dimensional position relative to the MRF and $\hat{u}_i^*$ is the fluid velocity relative to the MRF, $x_{\mathrm{mrf},i}^*$ and $u_{\mathrm{mrf},i}^*$ represents the absolute (lab) position and velocity of the MRF itself. For brevity, the asterisks are omitted in the remainder of this paper.

The motion of the MRF should follow that of the bubble to keep the bubble at its initial position relative to the MRF. Since the bubble motion is unknown a-priori a PID-controller is used that continuously update the acceleration of the MRF based on the error value $e_i(t) = \hat{x}_i^{\mathrm{b}}(t) - \hat{x}_i^{0,\mathrm{b}}$, that represent the distance between the bubble centre of mass and the initial bubble position in the MRF, and the velocity of the bubble relative to the MRF $\dfrac{de_i}{dt}$. The acceleration and velocity of the MRF are determined as

$$a_{\mathrm{mrf},i}(t) = K_{P,i}\left(e_i + \frac{1}{T_{I,i}}\int_0^t e_i(t')dt' + T_{D,i}\frac{de_i}{dt}\right), \tag{9}$$

$$u_{\mathrm{mrf},i}(t) = u_{\mathrm{mrf},i}^0 + \int_0^t a_{\mathrm{mrf},i}(t')dt' \,, \tag{10}$$

where $u_{\mathrm{mrf},i}^0$ is the initial velocity of the MRF and $K_{\mathrm{P},i}$, $T_{\mathrm{I},i}$ and $T_{\mathrm{D},i}$ are the i^{th} component of the proportional, integral and derivative coefficients, respectively. Using the heuristic and systematic Ziegler-Nichols tuning method [18, 19], the obtained parameters are ($K_{\mathrm{P},i} = 330$, $T_{\mathrm{I},i} = 0.2$ and $T_{\mathrm{D},i} = 0.13$) that produce stable regulations and minor bubble displacements $e_i(t)$ for all our simulations.

An unsteady velocity field is imposed, in the microscopic solver, that is obtained by sampling the external undisturbed turbulent liquid velocity and gradient tensor at the Lagrangian bubble position $x_i^{\mathrm{b}}(t)$ in the macroscopic solver. Assuming the bubble to be smaller than or comparable with the Kolmogorov length scale, the liquid velocity field surrounding the bubble can be approximated as linear [20]. With a first-order Taylor's expansion, this flow field is defined as:

$$U_i^{(1)}(\hat{x}_i, t) = u_i^{\mathrm{e,b}}(t) + \frac{\partial u_i^{\mathrm{e,b}}}{\partial \hat{x}_j}(t)(\hat{x}_j - \hat{x}_j^{\mathrm{b}}) \,, \tag{11}$$

where $u_i^{\mathrm{e,b}}(t)$ is the absolute velocity and $\dfrac{\partial u_i^{\mathrm{e,b}}}{\partial \hat{x}_i}(t)$ is the gradients of the undisturbed liquid velocity field at $x_i^{\mathrm{b}}(t)$ extracted from the macroscale simulations. $\hat{x}_j^{\mathrm{b}}$ is the position of the bubble in the MRF.

The linearised field $U_i^{(1)}(\hat{x}_i, t)$ is imposed on the microscopic solver by continuously updating the boundary conditions $\hat{u}_{\mathrm{BC},i}(\hat{x}_j, t) = U_i^{(1)}(\hat{x}_j, t) - u_{\mathrm{mrf},i}(t)$ and by correspondingly accelerate the microscopic flow field according to

$$a_{U,i}^{(1)}(\hat{x}_i, t) = \frac{d}{dt}(u_i^{\mathrm{e,b}}) + \frac{d}{dt}\left(\frac{\partial u_i^{\mathrm{e,b}}}{\partial \hat{x}_j}\right)(\hat{x}_j - \hat{x}_j^{\mathrm{b}}) \,. \tag{12}$$

The Volume of Fluid (VOF) numerical approach is used to solve the microscopic two-phase flow problem [21]. The governing equations in the MRF are the non-dimensional incompressible Navier-Stokes equations and the advection of the volume fraction field c:

$$\frac{\partial \hat{u}_i}{\partial \hat{x}_i} = 0 \,, \tag{13}$$

$$\rho\left(\frac{\partial \hat{u}_i}{\partial \hat{t}} + \hat{u}_j\frac{\partial \hat{u}_i}{\partial \hat{x}_j}\right) = \rho\left(g_i - a_{\mathrm{mrf},i} + a_{U,i}^{(1)}\right) + \\ -\frac{\partial p}{\partial \hat{x}_i} + \frac{1}{Ga}\frac{\partial}{\partial \hat{x}_j}\left(\mu\left(\frac{\partial \hat{u}_i}{\partial \hat{x}_j} + \frac{\partial \hat{u}_j}{\partial \hat{x}_i}\right)\right) + \frac{\hat{\kappa}\delta_S \hat{n}_i}{Eo} \,, \tag{14}$$

$$\frac{\partial c}{\partial \hat{t}} + \frac{\partial c\hat{u}_i}{\partial \hat{x}_i} = 0 \,, \tag{15}$$

where δ_S is the Dirac distribution function, κ and n_i are the interface curvature and the normal vector. The extra acceleration terms in Eq. 14 represents the acceleration due to the motion of the MRF and the unsteady external velocity field given by the macroscale framework. The VOF method is a one-fluid formulation where the fluid density ρ and viscosity μ varies according to

$$\rho(c) = c\rho_l + (1-c)\rho_g \,, \tag{16}$$

$$\mu(c) = \left(\frac{c}{\mu_l} + \frac{1-c}{\mu_g}\right)^{-1} \,, \tag{17}$$

where a harmonic mean is used to for the viscosity since that is generally more accurate for gas-liquid interfaces with a continuous shear stress [22]. The governing equations are solved with the open-source code Basilisk on a tree-structured Cartesian grid with an efficient adaptive grid refinement technique [23, 24].

2.3. Case setup

The multiscale framework is used to simulate a rising bubble in a turbulent liquid flow. With the macroscale pseudo-spectral solver, homogeneous isotropic turbulence is simulated at the Taylor Reynolds number $Re_\lambda = u_{\mathrm{rms}}\lambda/\nu = 180$. Here, u_{rms} is the root mean square of the velocity fluctuations and $\lambda = \sqrt{\varepsilon/15\nu u_{\mathrm{rms}}}$ is the Taylor length scale. The computational domain is cubical with the side length $2\pi^3$

and a spatial resolution of 256^3 grid points. Periodic boundary conditions are used in all three directions. With water as the liquid and assuming a turbulent dissipation rate of 1.5 10^{-5} m^2/s^3, the Kolmogorov length scale becomes 0.5 *mm*, the spherical bubble diameter is 0.76 *mm* and the time scale is 0.26 *s*. In non-dimensional form, the Kolmogorov length scale is 0.015 and the Kolmogorov time becomes 0.35.

In the microscopic framework the parameter $Ga = 65$ is used that corresponds to the 0.76 *mm* air bubble in water. To study the effects of different bubble deformations the cases $Eo = (10, 30, 50, 120)$ are simulated that corresponds to the air bubble but with a reduced surface tension. A cubic computational domain of $(10D)^3$ is specified where the bubble is kept in the centre by the PID-controlled MRF technique and an unsteady external velocity field is imposed based on the signal from the macroscopic simulation according to Eq. 11. The adaptive grid refinement technique in Basilisk is used to obtain sufficient grid refinement in regions containing the interface and with relatively high values of the second gradient of the velocity field. The maximum grid resolution corresponds to more than 50 cells/D.

3. SIMULATION RESULTS

A snapshot from the microscopic simulation case with $Ga = 65$ and $Eo = 50$ is shown in Figure 2. Here, the bubble is kept in the centre of the computational domain by the PID-controlled MRF technique and the external fluctuating liquid velocity field predicted by the macroscopic solver is imposed as described in Section 2.2. The contours represent the velocity magnitude relative to the MRF made non-dimensional by the characteristic velocity scale $\sqrt{gD}$. Throughout the simulation, the orientation angle ϕ is computed, defined as the angle between the bubble minor axis a and the vertical y-axis, and the bubble aspect ratio $\chi = b/a$ defined as the ratio of the major, b, to minor bubble axes. ϕ and χ are computed using the approach by [25] where χ is defined as the ratio of the larger to the smaller eigenvalues, $\chi \approx (I_{\max}/I_{\min})^{1/2}$, of the second moment of inertia tensor

$$I_{ij} = \frac{1}{m^{\mathrm{b}}} \int_{\Omega^{\mathrm{b}}} (\hat{x}_i - \hat{x}_i^{\mathrm{b}})(\hat{x}_j - \hat{x}_j^{\mathrm{b}}) \rho_{\mathrm{g}} d\hat{V}\,, \tag{18}$$

where Ω^b is the bubble volume.

Figure 3 shows how the χ, ϕ and instantaneous bubble drag force coefficient C_{D} vary in the microscopic simulations. All simulations are stopped at $t/\tau_\eta = 4$ and the same unsteady external velocity field signal is imposed on all cases.

The top panel shows the modulus of the imposed velocity field strain rate tensor $|S^{\mathrm{e}}_{ij}| = \sqrt{S^{\mathrm{e}}_{ij} S^{\mathrm{e}}_{ij}}$, ($S^{\mathrm{e}}_{ij}$ is the symmetric part of the imposed velocity gradient $\partial u_i^{\mathrm{e,b}}/\partial \hat{x}_j$ obtained at the bubble position in the macroscopic simulation). This quantity gives a representation of a typical turbulent signal for the gradients with large localised peaks. The second panel of Fig. 3 shows how the bubble aspect ratio χ vary in response to the imposed fluctuating velocity field and due to unsteady small-scale bubble dynamics such as shape and trajectory oscillations. The case $Eo = 10$ corresponds to the case with the highest relative surface tension force and results in a $\chi \in [3.0, 3.2]$ during the simulation. This case show a correlation between the imposed strain rate $|S^{\mathrm{e}}_{ij}|$ and χ with a Pearson's correlation coefficient of 0.5 in the interval $t/\tau_\eta = [0.5, 4]$. The cases $Eo = 30$ and $Eo = 50$ are, however, not well correlated with $|S^{\mathrm{e}}_{ij}|$ and show fluctuations of χ that are characterised by time scales smaller than the Kolmogorov time scale. At $Eo = 30$, χ is overall larger than for $Eo = 10$ and fluctuate roughly between $[3, 4]$. However, at $Eo = 50$, χ decreases and fluctuates around $[2, 3]$. That χ is the lowest for the highest Eo-number can be explained by the definition of χ and the change of characteristic bubble shapes with reduced surface tension illustrated in Figure 4. Here, the bubble shape for $Eo = 50$ is close to a spherical cap that have a lower aspect ratio than the oblate spheroid shape at $Eo = 10$. At $Eo = 120$, the surface tension is too low to keep the bubble intact and a peripheral breakup occur. Because of the breakup, no quantitative data are presented for the $Eo = 120$ case.

The third panel of Fig. 3 shows the orientation angle ϕ and clearly indicate that the different Eo-numbers result in different oscillating behaviors. The fastest oscillations, in the case $Eo = 30$, are around an order of magnitude faster than the Kolmogorov time scale τ_η and are more related to the capillary time scale [26] $\tau_\sigma = \sqrt{\rho_{\mathrm{l}} D^3/\sigma} \approx 0.2\tau_\eta$ indicating that bubble shape oscillations significantly influence the bubble motion for this case.

The bottom panel of Fig. 3 shows the instantaneous bubble drag force coefficient that fluctuates at around $C_{\mathrm{D}} \approx 2$ for the case $Eo = 10$ but increase to $C_{\mathrm{D}} \approx 3$ for the $Eo = 30$ and $Eo = 50$ cases. This 50% drag coefficient increase is related to the change of bubble shapes at different Eo-numbers. Fig. 4 shows the characteristic shapes of the bubbles during the simulations. At $Eo = 10$, the bubble is approximately an oblate spheroid with a lower C_D than the cases $Eo = 30$ and $Eo = 50$ that are closer to a spherical cap shape.

That C_{D} oscillate in the case $Eo = 30$ can be explained by the aforementioned bubble shape oscillations and the bubble trajectory in the absolute, or lab, reference frame shown in Figure 5. Although the bubble shape and trajectory at $Eo = 30$ is similar to $Eo = 50$, the former case has the oscillating shape and a spiralling trajectory (seen as oscillations of the trajectory in Fig. 5) that cause the instantaneous C_{D} to vary. Since the time-averaged C_{D} is similar for both $Eo = 30$ and $Eo = 50$, the overall trajectories for both cases become similar. In the case $Eo = 10$, the C_{D} is lower and therefore this bubble travels further in the y-direction.

By performing a time lagged cross correlation

between the $|S^{e}_{ij}|(t)$ and $C_D(t)$ a peak Pearson's correlation coefficient is obtained when C_D lags about $t/\tau_\eta \approx 0.2$, or, in the capillary time scale $t/\tau_\sigma = O(1)$, for all cases (the $C_D(t)$ signal is shifted back $t/\tau_\eta \approx 0.2$). At this time lag, the correlation coefficient is about 0.3 for $Eo = 10$, 0.2 for $Eo = 30$ and 0.15 for $Eo = 50$. These values indicate the C_D is correlated with the imposed fluctuating strain rates but with a response time of $t/\tau_\sigma = O(1)$ implying that capillary effects are governing the response dynamics.

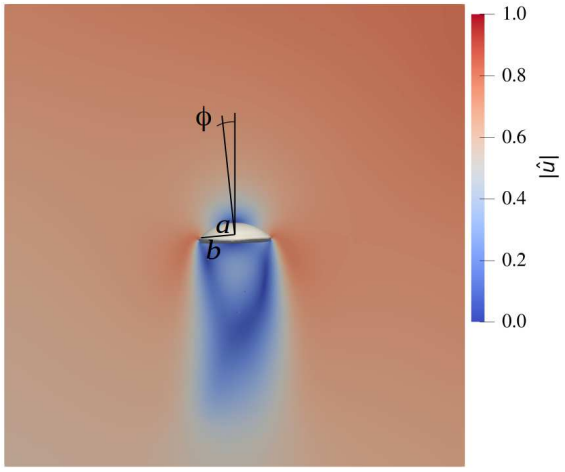

Figure 2. Snapshot of the velocity magnitude relative to the MRF, normalised with the characteristic velocity scale $\sqrt{gD}$, in the simulation case $Ga = 65, Eo = 50$. The angle between the bubble minor axis a and the vertical y-axis is defined as the orientation angle ϕ. The ratio of the major b and minor a semi-axes is the bubble aspect ratio $\chi = b/a$.

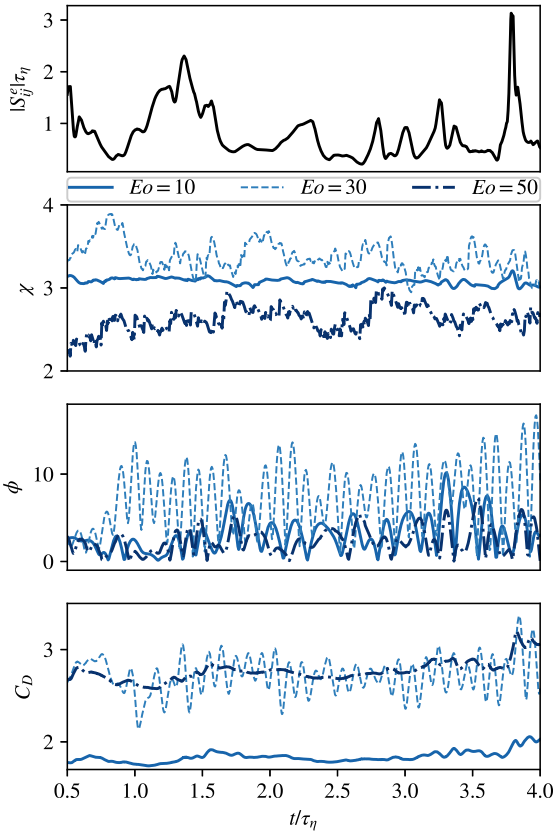

Figure 3. Evolution of the modulus of the external velocity field strain rate (top panel), the bubble aspect ratio (second panel), the bubble orientation angle (third panel) and the instantaneous bubble drag force coefficient (bottom panel). The modulus of the strain rate is the same for all simulation cases while the evolution of the other bubble properties (in the three bottom panels) change with the Eo number. The legend above the second panel applies to all three bottom panels.

4. CONCLUSIONS

In this paper, a multiscale numerical framework is formulated that handles bubbles or droplets with diameters comparable to, or smaller than, the Kolmogorov length scale and with arbitrary density ratios to the carrier phase. A PID-controlled moving reference frame technique is used to follow the motion of bubbles or droplets with high relative velocities to the carrier phase due to gravitational forces. The fluctuating external velocity field is efficiently imposed on the bubble microscale solver by adding body forces proportional to the time derivatives of the linearised external velocity field. This imposition method improves the efficiency of the algorithm by at least two orders of magnitudes compared with the framework suggested by [8].

The multiscale numerical framework resolves the effects of both large-scale turbulent fluctuations and small-scale phenomena such as bubble induced flow disturbances and capillary effects. The simulations capture bubble dynamics that are at least an order of magnitude faster than the Kolmogorov time scale. In particular, the results show significant changes in the small-scale bubble dynamics by varying the surface tension. The relative importance of the surface tension also influence how several bubble properties correlate with the imposed external strain rate. These results illustrate the ability of the proposed multiscale framework to resolve and study both the bubble deformations induced by turbulent fluctuations and the small-scale bubble dynamics associated with capillary effects.

The numerical framework is presented in a general way so that it can be used with any DNS technique for two-phase flows (VOF, level-set, lattice-Boltzmann, diffuse interface approach). In future works, the multiscale framework can be further improved by running the two solvers in parallel. Then, the turbulent fluctuations from the macroscale simulation can be computed along the bubble trajectory given by the microscale simulation. This extension would provide a complete two-way coup-

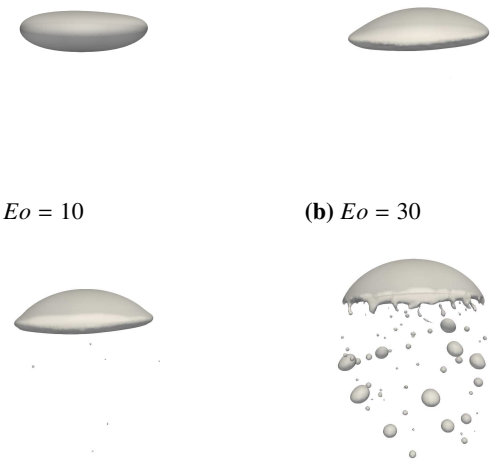

(a) $Eo = 10$ **(b)** $Eo = 30$

(c) $Eo = 50$ **(d)** $Eo = 120$

Figure 4. Characteristic bubble shapes in cases where a bubble rise in homogeneous isotropic turbulence. The same simulation setup and turbulent field is used in all cases but an increasing Eo number is specified that reduce the relative importance of the surface tension force. At increasing Eo-number, the bubble is more deformed and, at $Eo = 120$, a peripheral breakup occurs.

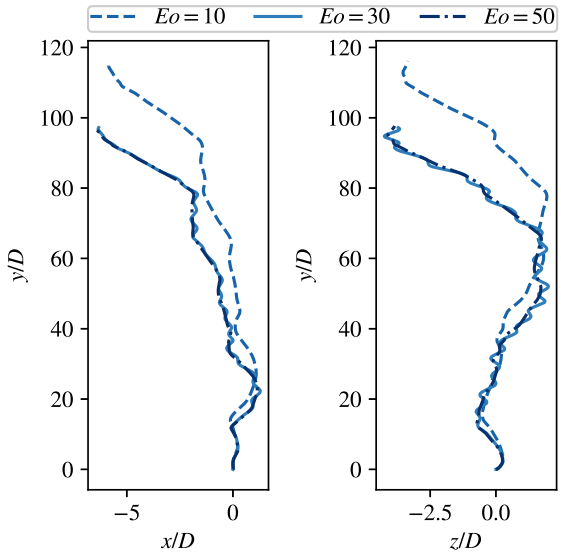

Figure 5. Bubble trajectories in an absolute, or lab, reference frame predicted by the microscale simulation in the x/y-plane (left panel) and the z/y-plane (right panel). The same turbulent fluctuations are imposed on all simulations but the different Eo-numbers results in different small-scale bubble dynamics that influence the trajectory.

ling between the small-scale bubble dynamics and the large-scale turbulent field.

ACKNOWLEDGEMENTS

We acknowledge support from the Swedish Research Council (Vetenskapsrådet), grant VR 2017-05031. The computations were performed using resources provided by the Swedish National Infrastructure for Computing (SNIC) at NSC partially funded by the Swedish Research Council through grant agreement no. 2018-05973.

REFERENCES

[1] Mudde, R. F., 2005, "Gravity-driven bubbly flows", *Annu Rev Fluid Mech*, Vol. 37, pp. 393–423.

[2] Magnaudet, J., and Eames, I., 2000, "The motion of high-Reynolds-number bubbles in inhomogeneous flows", *Annual Review of Fluid Mechanics*, Vol. 32 (1), pp. 659–708.

[3] Hidman, N., Ström, H., Sasic, S., and Sardina, G., 2022, "A multiscale methodology for small-scale bubble dynamics in turbulence", *International Journal of Multiphase Flow*, p. 103976.

[4] van der Hoef, M. A., van Sint Annaland, M., Deen, N., and Kuipers, J., 2008, "Numerical simulation of dense gas-solid fluidized beds: a multiscale modeling strategy", *Annual Review of Fluid Mechanics*, Vol. 40, pp. 47–70.

[5] Bunner, B., and Tryggvason, G., 1999, "Direct numerical simulations of three-dimensional bubbly flows", *Physics of Fluids*, Vol. 11 (8), pp. 1967–1969.

[6] Tripathi, M. K., Sahu, K. C., and Govindarajan, R., 2014, "Why a falling drop does not in general behave like a rising bubble", *Scientific Reports*, Vol. 4, p. 4771.

[7] Cano-Lozano, J. C., Martinez-Bazan, C., Magnaudet, J., and Tchoufag, J., 2016, "Paths and wakes of deformable nearly spheroidal rising bubbles close to the transition to path instability", *Physical Review Fluids*, Vol. 1 (5), p. 053604.

[8] Milan, F., Biferale, L., Sbragaglia, M., and Toschi, F., 2020, "Sub-Kolmogorov droplet dynamics in isotropic turbulence using a multiscale lattice Boltzmann scheme", *Journal of Computational Science*, Vol. 45, p. 101178.

[9] Maxey, M. R., and Riley, J. J., 1983, "Equation of motion for a small rigid sphere in a nonuniform flow", *The Physics of Fluids*, Vol. 26 (4), pp. 883–889.

[10] Lörstad, D., and Fuchs, L., 2004, "High-order surface tension VOF-model for 3D bubble

flows with high density ratio", *Journal of Computational Physics*, Vol. 200 (1), pp. 153–176.

[11] Lörstad, D., Francois, M., Shyy, W., and Fuchs, L., 2004, "Assessment of volume of fluid and immersed boundary methods for droplet computations", *International Journal for Numerical Methods in Fluids*, Vol. 46 (2), pp. 109–125.

[12] Rusche, H., 2002, "Computational fluid dynamics of dispersed two-phase flows at high phase fractions", Ph.D. thesis, University of London.

[13] Fan, Y., Fang, J., and Bolotnov, I., 2021, "Complex bubble deformation and break-up dynamics studies using interface capturing approach", *Experimental and Computational Multiphase Flow*, Vol. 3 (3), pp. 139–151.

[14] Mei, R., and Klausner, J. F., 1992, "Unsteady force on a spherical bubble at finite Reynolds number with small fluctuations in the free-stream velocity", *Physics of Fluids A: Fluid Dynamics*, Vol. 4 (1), pp. 63–70.

[15] Spandan, V., Ostilla-Mónico, R., Verzicco, R., and Lohse, D., 2016, "Drag reduction in numerical two-phase Taylor–Couette turbulence using an Euler–Lagrange approach", *Journal of Fluid Mechanics*, Vol. 798, pp. 411–435.

[16] Sardina, G., Picano, F., Brandt, L., and Caballero, R., 2015, "Continuous growth of droplet size variance due to condensation in turbulent clouds", *Physical Review Letters*, Vol. 115 (18), p. 184501.

[17] Sardina, G., Jareteg, K., Ström, H., and Sasic, S., 2019, "Assessing the ability of the Eulerian-Eulerian and the Eulerian-Lagrangian frameworks to capture meso-scale dynamics in bubbly flows", *Chemical Engineering Science*, Vol. 201, pp. 58–73.

[18] Ziegler, J. G., Nichols, N. B., et al., 1942, "Optimum settings for automatic controllers", *trans ASME*, Vol. 64, p. 11.

[19] McCormack, A. S., and Godfrey, K. R., 1998, "Rule-based autotuning based on frequency domain identification", *IEEE transactions on control systems technology*, Vol. 6 (1), pp. 43–61.

[20] Pope, S. B., 2001, *Turbulent flows*, IOP Publishing.

[21] Benson, D. J., 2002, "Volume of fluid interface reconstruction methods for multi-material problems", *Applied Mechanics Reviews*, Vol. 55 (2), pp. 151–165.

[22] Tryggvason, G., Scardovelli, R., and Zaleski, S., 2011, *Direct numerical simulations of gas–liquid multiphase flows*, Cambridge University Press.

[23] Popinet, S., 2015, "A quadtree-adaptive multigrid solver for the Serre–Green–Naghdi equations", *Journal of Computational Physics*, Vol. 302, pp. 336–358.

[24] URL `http://basilisk.fr`.

[25] Bunner, B., and Tryggvason, G., 2003, "Effect of bubble deformation on the properties of bubbly flows", *Journal of Fluid Mechanics*, Vol. 495, p. 77.

[26] Popinet, S., 2018, "Numerical models of surface tension", *Annual Review of Fluid Mechanics*, Vol. 50, pp. 49–75.